Acta Cryst E CRYSTALLOGRAPHIC COMMUNICATIONS

ISSN 2056-9890

Crystal structure of binimetinib (Form A), $C_{17}H_{15}BrF_2N_4O_3$, from synchrotron X-ray powder diffraction data and density functional theory

Jean guillaume Ducreux,[a] James A. Kaduk,[a]* Anja Dosen[b] and Thomas N. Blanton[b]

[a]Department of Chemistry, North Central College, 131 S. Loomis, St., Naperville IL, 60540, USA, and [b]ICDD, 12 Campus Blvd., Newtown Square PA, 19073, USA. *Correspondence e-mail: kaduk@polycrystallography.com

Received 23 March 2026
Accepted 6 May 2026

Edited by W. T. A. Harrison, University of Aberdeen, United Kingdom

Keywords: powder diffraction; binimetinib; Mektovi; Rietveld refinement; density functional theory.

CCDC references: 2552042; 2552043; 2552044; 2552045

Supporting information: this article has supporting information at journals.iucr.org/e

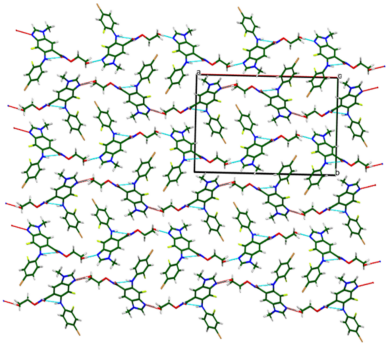

The crystal structure of binimetinib Form A [systematic name: 6-(4-bromo-2-fluoroanilino)-7-fluoro-*N*-(2-hydroxyethoxy)-3-methylbenzimidazole-5-carboxamide], $C_{17}H_{15}BrF_2N_4O_3$, has been solved and refined using synchrotron X-ray powder diffraction data, and optimized using density functional theory techniques. It crystallizes in space group $P2_12_12_1$ with one molecule in the asymmetric unit at 298 K. The crystal structure consists of layers of molecules lying parallel to the *bc* plane. Hydrogen bonds (O/N—H···N/O) link the layers *via* sheets in the *ac* plane. The commercial sample contains minor impurities of $KH_2(PO_4)$ and $Fe_{0.33}Zr_2(PO_4)_3$.

1. Chemical context

Binimetinib, $C_{17}H_{15}BrF_2N_4O_3$, sold under the brand name Mektovi, is an anti-cancer medication (Tran & Cohen, 2020). Administered orally, binimetinib is combined with encorafenib for the treatment of melanoma. Its systematic name (CAS Registry Number 606143-89-9) is 6-(4-bromo-2-fluoroanilino)-7-fluoro-*N*-(2-hydroxyethoxy)-3-methylbenzimidazole-5-carboxamide.

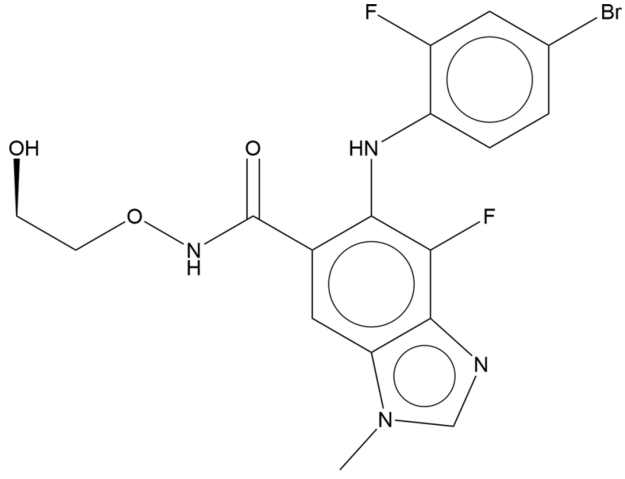

This work was carried out as part of a project (Kaduk *et al.*, 2014) to determine the crystal structures of large-volume commercial pharmaceuticals, and include high-quality powder diffraction data for them in the Powder Diffraction File (Kabekkodu *et al.*, 2024).

2. Structural commentary

The powder pattern obtained in this study is similar enough to the one reported for binimetinib Form A by Chen *et al.* (2016)

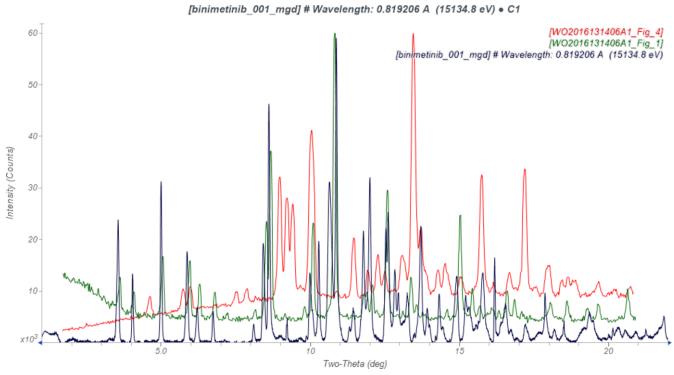

Figure 1
Comparison of the background-subtracted synchrotron pattern of binimetinib (black) to those for Form A (green) and Form B (red) reported by Chen *et al.* (2016). The patent patterns (measured using Cu *Kα* radiation) were digitized using *UN-SCAN-IT* (Silk Scientific, 2013) and converted to the synchrotron wavelength of 0.819325 (2) Å using *JADE Pro* (MDI, 2025). Image generated using *JADE Pro* (MDI, 2025).

to conclude that they are the same material (Fig. 1). There are extra peaks in the synchrotron pattern indicating the presence of at least two crystalline impurities, which we have identified as 2.6% $KH_2(PO_4)$ and approximately 0.3% $Fe_{0.33}Zr_2(PO_4)_3$. It would be interesting to understand how these phases came to be present in this commercial sample.

The root-mean-square difference of the non-H atoms in the Rietveld-refined and *VASP*-optimized structures of binimetinib, calculated using the *Mercury* CSD-Materials/Search/Crystal Packing similarity tool (Macrae *et al.*, 2020) is 0.549 Å (Fig. 2). The root-mean-square Cartesian displacement of the non-H atoms in the refined and optimized structures, calculated using the *Mercury* Calculate/Molecule overlay tool, is 0.392 Å (Fig. 3). The largest differences are in the side chains. The agreements are just outside the normal range for correct structures (van de Streek & Neumann, 2014). Since the specimen was almost certainly changing due to exposure to the synchrotron beam, the accuracy of this structure might be

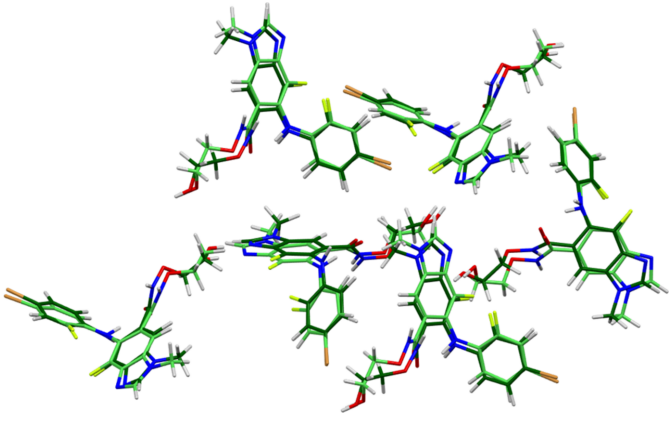

Figure 2
Comparison of the Rietveld-refined (colored by atom type) and *VASP*-optimized (light green) structures of binimetinib using the *Mercury* CSD-Materials/Search/Crystal Packing Similarity tool. The root-mean-square Cartesian displacement is 0.549 Å. Image generated using *Mercury* (Macrae *et al.*, 2020).

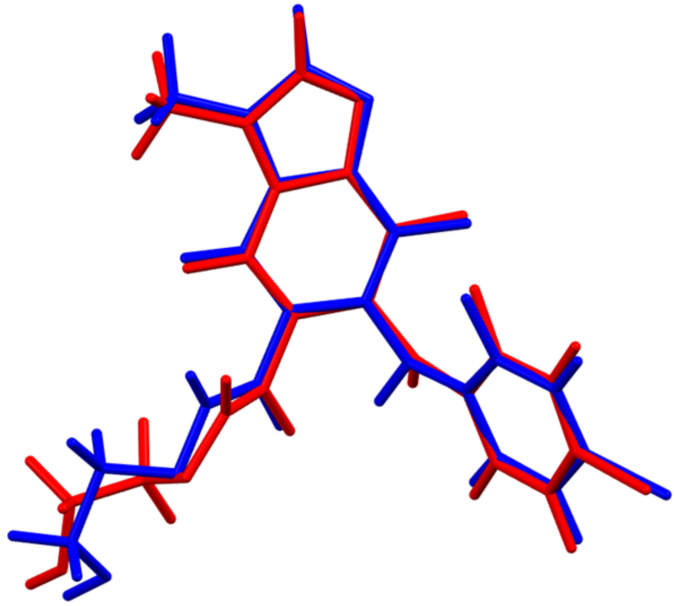

Figure 3
Comparison of the refined structure of binimetinib (red) to the *VASP*-optimized structure (blue). The comparison was generated using the *Mercury* Calculate/Molecule Overlay tool; the r.m.s. difference is 0.392 Å. Image generated using *Mercury* (Macrae *et al.*, 2020).

lower than usual. The asymmetric unit is illustrated in Fig. 4. The remaining discussion will emphasize the *VASP*-optimized structure.

All of the bond distances, and most of the bond angles and torsion angles fall within the normal ranges indicated by a *Mercury* Mogul geometry check (Macrae *et al.*, 2020). The C21—C20—N8 bond angle [126.1°; average = 118.9 (22)°; *Z*-score = 3.2] is flagged as unusual. Torsion angles involving rotation about the N8—C20 bond are flagged as unusual. They

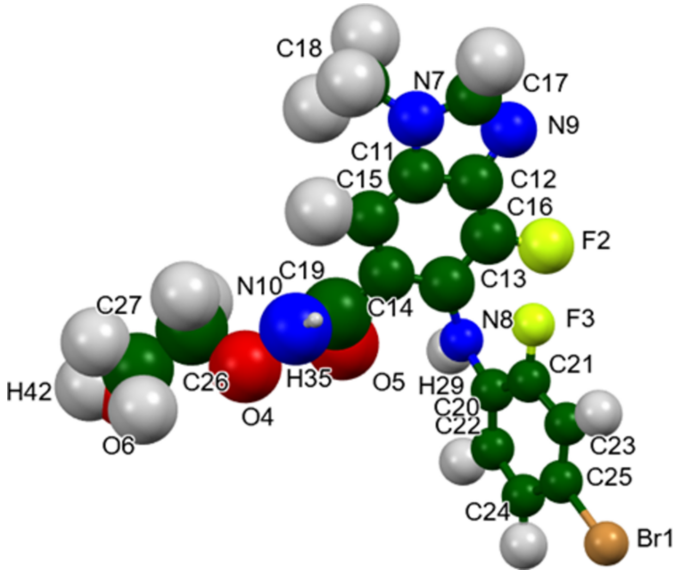

Figure 4
The asymmetric unit of binimetinib, with the atom numbering. The atoms are represented by 50% probability spheroids. Image generated using *Mercury* (Macrae *et al.*, 2020).

lie on long tails of the distributions of similar torsion angles, so are unusual but not unprecedented. The O4—C26—C27—O5 torsion angle of −62.9° indicates a *gauche* conformation for the hydroxyethyl side chain and the dihedral angle between the benzimidazole and phenyl ring mean planes is 57.0°.

Quantum chemical geometry optimization of the isolated binimetinib molecule (DFT/B3LYP/6-31G*/water) using *Spartan '24* (Wavefunction, 2025) indicated that the observed conformation is 6.2 kcal mol^{-1} higher in energy than the local minimum. The root-mean-square difference is 0.410 Å, and the maximum differences are in the amide group. The global minimum-energy conformation has a similar energy, but is much more compact (severely folded on itself). The molecule is apparently flexible, and intermolecular interactions are important in determining the solid-state conformation.

3. Supramolecular features

The extended structure (Fig. 5) consists of layers lying parallel to the *bc* plane. Hydrogen bonds (O/N—H···N/O) link the layers *via* sheets in the *ac* plane. Analysis of the contributions to the total crystal energy of the structure using the Forcite module of Materials Studio (Dassault Systèmes, 2024) indicated that the intramolecular energy is dominated by angle distortion terms. The intermolecular energy is dominated by van der Waals attractions, which in this force field based analysis include hydrogen bonds. The hydrogen bonds are better discussed using the results of the DFT calculation.

Hydrogen bonds (Table 1) are prominent in the structure. The O6—H42···N9, N10—H35···O5, and N8—H29···O5 hydrogen bonds link the molecules into sheets lying parallel to the *ac* plane. The energies of the N—H···O bonds were calculated using the correlation of Wheatley & Kaduk (2019).

Table 1
Hydrogen-bond geometry (Å, °).

D—H···*A*	*D*—H	H···*A*	*D*···*A*	*D*—H···*A*
N8—H29···O5	1.02	1.90	2.727	136
N10—H35···O5^{i}	1.04	1.67	2.675	161
O6—H42···N9^{ii}	1.00	1.81	2.806	176
C17—H30···O6^{iii}	1.09	2.18	3.221	158
C18—H32···O5^{iii}	1.10	2.53	3.288	125
C26—H38···Br1^{iv}	1.10	2.92	3.841	142
C26—H39···Br1^{iii}	1.10	2.78	3.486	122

Symmetry codes: (i) $x, y, z-1$; (ii) $x-\frac{1}{2}, -y+\frac{3}{2}, -z+1$; (iii) $-x, y-\frac{1}{2}, -z+\frac{1}{2}$; (iv) $-x, y-\frac{1}{2}, -z+\frac{3}{2}$.

The O6—H42···N9 bond generates a graph-set descriptor (Etter, 1990; Bernstein *et al.*, 1995; Motherwell *et al.*, 2000) $C_1^1(12)$ and the N10—H35···O5 bond corresponds to graph set $C_1^1(4)$. Several C—H···O hydrogen bonds also contribute to the cohesion of the structure. By the Mulliken overlap population criterion, the C17—H30···O6 bond is exceptionally strong.

The volume enclosed by the Hirshfeld surface of binimetinib (Fig. 6; Hirshfeld, 1977; Spackman *et al.*, 2021) is 443.0 Å^3 or 98.1% of 1/4 of the unit-cell volume. The only significant close contacts (red in Fig. 6) involve the hydrogen bonds. The volume/non-hydrogen atom is smaller than usual, at 16.7 Å^3, so the packing seems relatively dense.

The Bravais–Friedel–Donnay–Harker (Bravais, 1866; Friedel, 1907; Donnay & Harker, 1937) algorithm suggests that we might expect needle morphology for binimetinib, with [001] as the long axis, as expected from the anisotropy of the lattice parameters. A photomicrograph (Fig. 7) indicates needle morphology. A 2nd-order spherical harmonic model was included for preferred orientation. The texture index was

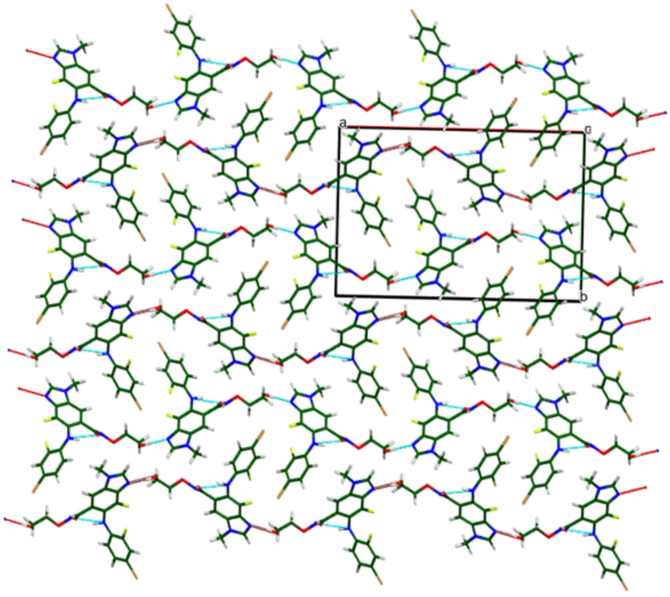

Figure 5
Crystal structure of binimetinib, viewed down the *c* axis. Image generated using *Mercury* (Macrae *et al.*, 2020).

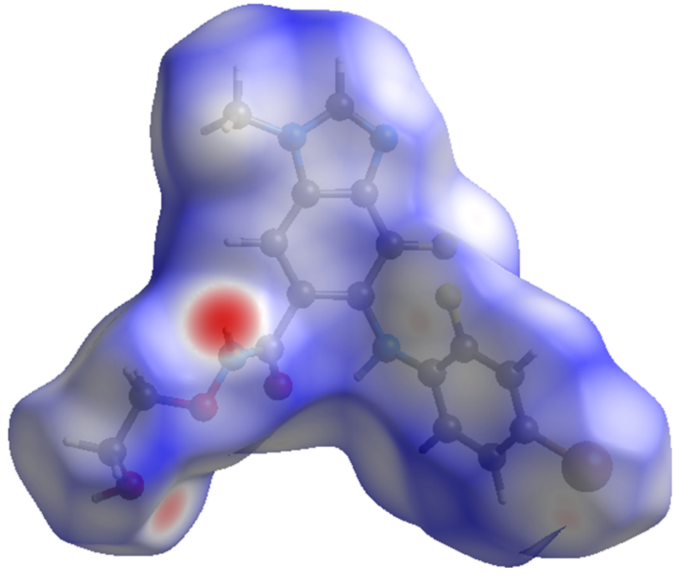

Figure 6
The Hirshfeld surface of binimetinib. Intermolecular contacts longer than the sums of the van der Waals radii are colored blue, and contacts shorter than the sums of the radii are colored red. Contacts equal to the sums of radii are white. Image generated using *CrystalExplorer* (Spackman *et al.*, 2021).

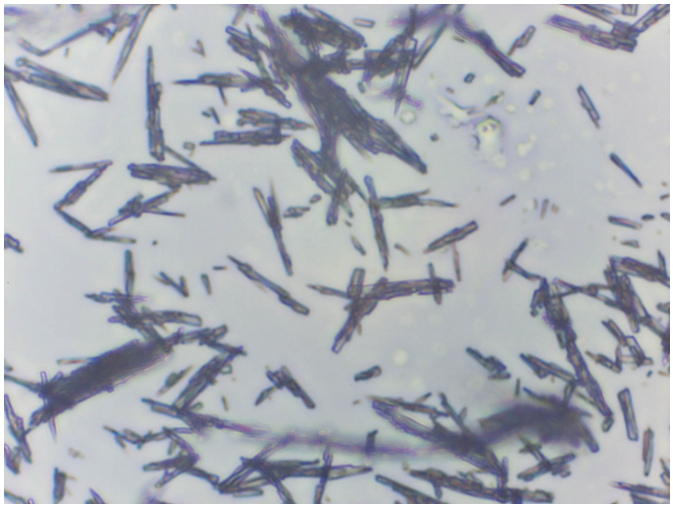

Figure 7
Optical micrograph of binimetinib. Original magnification = 40×.

1.048 (3), indicating that preferred orientation was significant in this rotated capillary specimen.

4. Database survey

Powder patterns for crystalline Forms A and B of binimetinib are reported in International Patent Application WO 2016/131406 A1 (Chen *et al.*, 2016; Crystal Pharmatech Co. Ltd.), but no crystal structures were reported. The crystal structure of a DMSO adduct of binimetinib has been determined (Buist *et al.*, 2021; Johnson Matthey Public Limited Company), and X-ray powder diffraction data are reported. Powder data are also reported for a citric acid adduct. A Raman spectrum for binimetinib free base is reported, but no diffraction data. Amorphous binimetinib is claimed in International Patent Application WO 2021/116901 A1 (Palle *et al.*, 2021; Biocon Ltd.). A reduced-cell search in the Cambridge Structural Database (CSD Conquest Build 2026.1.0; Groom *et al.*, 2016) yielded 15 hits for unrelated structures, but no structures for binimetinib or its derivatives.

5. Synthesis and crystallization

Binimetinib is a commercial reagent, purchased from TargetMol (Batch #146079), and was used as-received.

6. Refinement

Crystal data, data collection and structure refinement details are summarized in Table 2. The white powder was packed into a 0.5 mm diameter Kapton capillary, and rotated during the measurement at ∼2 Hz. The powder pattern was measured at 298 (1) K at the Wiggler Low Energy Beamline (Leontowich *et al.*, 2021) of the Brockhouse X-ray Diffraction and Scattering Sector of the Canadian Light Source using a wavelength of 0.819325 (2) Å (15.1 keV) from 1.6–75.0° 2θ with a step size of 0.0025° and a collection time of 3 minutes. The high-resolution powder diffraction data were collected using eight

Table 2
Experimental details.

Crystal data	
Chemical formula	$C_{17}H_{15}BrF_2N_4O_3$
M_r	441.23
Crystal system, space group	Orthorhombic, $P2_12_12_1$
Temperature (K)	298
a, b, c (Å)	23.1607 (11), 16.0073 (11), 4.86578 (17)
V (Å^3)	1803.9 (2)
Z	4
Radiation type	Synchrotron, λ = 0.81933 Å
Specimen shape, size (mm)	Cylinder, 0.45 × 0.15
Data collection	
Diffractometer	Wiggler Low Energy Beamline, Brockhouse X-ray Diffraction and Scattering Sector, Canadian Light Source
Specimen mounting	Kapton capillary
Data collection mode	Transmission
Scan method	Step
2θ values (°)	$2\theta_{min}$ = −9.008, $2\theta_{max}$ = 75.047, $2\theta_{step}$ = 0.003
Refinement	
R factors and goodness of fit	R_p = 0.011, R_{wp} = 0.018, R_{exp} = 0.001, χ^2 = 347.375
No. of parameters	113
No. of restraints	72
$(\Delta/\sigma)_{max}$	3.163

Computer programs: *GSAS-II* (Toby & Von Dreele, 2013).

Dectris Mythen2 X series 1K linear strip detectors. NIST SRM 660b LaB_6 was used to calibrate the instrument and refine the monochromatic wavelength used in the experiment.

Illuminating a Br-containing specimen with 15 keV X-rays results in severe fluorescent background (and thus eventually low residuals). It would be very surprising if this sample did not exhibit beam damage, as C—Br bonds are known to be prone to photolysis.

The pattern was difficult to index. Visual examination of the raw data indicated several very sharp peaks at high angles, probably indicating an inorganic impurity. Initial indexing using *N-TREOR* (Altomare *et al.*, 2013) yielded a $P2_1/c$ cell with a = 5.36109, b = 23.26552, c = 16.20200 Å, β = 95.864°, V = 2010.3 Å^3, and Z = 4. Although the structure could be solved and refined using this cell, the structure was unsatisfactory - both for the residuals (R_{wp} = 0.0267) and the agreement of observed and calculated peak positions, even considering potential beam damage.

Indexing with *DICVOL14* (Louër & Boultif, 2014), permitting up to three unindexed peaks, yielded a primitive monoclinic cell with a = 23.2656, b = 16.0153, c = 4.8916 Å, β = 90.420°, V = 1822.57 Å^3, and Z = 4. The β angle being close to 90° suggested that we consider the possibility that the cell was orthorhombic. The space-group-interpretation routine of *EXPO2014* (Altomare *et al.*, 2013) suggested space group $P2_12_12_1$, which was confirmed by successful solution and refinement of the structure.

The molecular structure of binimetinib was downloaded from PubChem (Kim *et al.*, 2023) as Conformer3D_COM-

POUND_CID_10288191.sdf. It was converted to a *.mol2 file using *Mercury* (Macrae *et al.*, 2020), and to a Fenske–Hall *Z*-matrix using *OpenBabel* (O'Boyle *et al.*, 2011). The crystal structure was solved by Monte Carlo simulated annealing techniques as implemented in *EXPO2014* (Altomare *et al.*, 2013) using the binimetinib molecule as the fragment, including a bump penalty on the non-H atoms and (001) preferred orientation. For the structure solution, a constant 49,000 counts were subtracted from the raw data, to minimize the effect of the high background. The structure was also solved using parallel tempering techniques as implemented in *FOX* (Favre-Nicolin & Černý, 2002), including (001) preferred orientation. Essentially the same structure was obtained from the two programs, and the *FOX* solution was adopted for refinement.

Indexing the sharp high-angle peaks using *DICVOL14* yielded a primitive tetragonal cell with a = 7.4557, c = 6.9776 Å, and V = 387.87 Å^3. A reduced cell search in the Powder Diffraction File yielded several metallic phases, as well as (orthorhombic) KH_2PO_4 (PDF entry 04-016-0040; Baur, 1973). Including this phase in the refinement revealed the presence of additional peaks, which are best accounted for by a zirconium phosphate phase such as $Fe_{0.33}Zr_2(PO_4)_3$ (PDF entry 04-015-1781; Gobechiya *et al.*, 2004), which was included as a third phase.

Rietveld refinement was carried out with *GSAS-II* (Toby & Von Dreele, 2013). Only the 3.3–35.0° portion of the pattern was included in the refinements (d_{min} = 1.362 Å). All non-H bond distances and angles were subjected to restraints, based on a *Mercury* Mogul Geometry Check (Sykes *et al.*, 2011; Bruno *et al.*, 2004). The Mogul average and standard deviation for each quantity were used as the restraint parameters. The aromatic rings were restrained to be planar. The restraints contributed 7.5% to the overall χ^2. The hydrogen atoms were included in calculated positions, which were recalculated during the refinement using *Materials Studio* (Dassault Systèmes, 2024). The U_{iso} were grouped by chemical similarity. An attempt to refine the Br atom anisotropically yielded a non-positive-definite ellipsoid, and so was abandoned. The peak profiles were described using the generalized microstrain model (Stephens, 1999). The background was modeled using a six-term shifted Chebyshev polynomial, with a peak at 11.21° to model the scattering from the Kapton capillary and any amorphous component of the sample.

The final refinement of 113 variables using 12,681 observations and 72 restraints yielded the residual R_{wp} = 0.01891. The largest peak (1.62 Å from F2) and hole (1.92 Å from O6) in the difference-Fourier map are 0.33 (9) and −0.31 (9) e Å^{-3}, respectively. The final Rietveld plot is shown in Fig. 8. The largest features in the normalized error plot are in the positions of some of the strong low-angle peaks, and probably indicate beam damage.

The crystal structure of binimetinib was optimized (fixed experimental unit cell) with density functional theory techniques using *VASP* (Kresse & Furthmüller, 1996) through the *MedeA* graphical interface (Materials Design, 2024). The calculation was carried out on 32 cores of a 144-core (768 Gb memory) HPE Superdome Flex 280 Linux server at North Central College. The calculation used the GGA-PBE functional, a plane wave cutoff energy of 400.0 eV, and a k-point spacing of 0.5 Å^{-1} leading to a 3 × 3 × 1 mesh, and took ∼7.4 h. Single-point density functional theory calculations and population analysis were carried out using *CRYSTAL23* (Erba *et al.*, 2023) (fixed experimental cell) and population analysis was carried out using *CRYSTAL17* (Dovesi *et al.*, 2018), using a fixed experimental cell. The basis sets for the H, C, N and O atoms in the calculation were those of Gatti *et al.* (1994), and those for Br and F were from Peintinger *et al.* (2013). The calculations were run on a 3.5 GHz PC using 8 k-points and the B3LYP functional, and took ∼2.1 hr

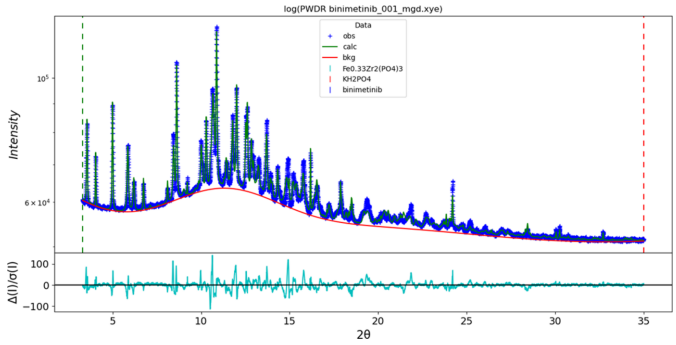

Figure 8
The Rietveld plot for binimetinib. The blue crosses represent the observed data points, and the green line is the calculated pattern. The cyan curve is the normalized error plot, and the red line is the background curve. The vertical scale is logarithmic.

Acknowledgements

Part of the research described in this paper was performed at the Canadian Light Source, a national research facility of the University of Saskatchewan, which is supported by the Canada Foundation for Innovation (CFI), the Natural Sciences and Engineering Research Council (NSERC), the Canadian Institute of Health Research (CIHR), the Government of Saskatchewan, and the University of Saskatchewan. We thank Adam Leontowich for his assistance in the data collection. We also thank the ICDD team – Megan Rost, Steve Trimble, and Dave Bohnenberger - for their contribution to research, sample preparation, and in-house XRD data collection and verification.

Funding information

Funding for this research was provided by: International Centre for Diffraction Data (grant No. 09-03).

References

Altomare, A., Cuocci, C., Giacovazzo, C., Moliterni, A., Rizzi, R., Corriero, N. & Falcicchio, A. (2013). *J. Appl. Cryst.* **46**, 1231–1235.
Baur, W. H. (1973). *Acta Cryst.* B**29**, 2726–2731.

Bernstein, J., Davis, R. E., Shimoni, L. & Chang, N. L. (1995). *Angew. Chem. Int. Ed. Engl.* **34**, 1555–1573.
Bravais, A. (1866). *Etudes Cristallographiques.* Paris: Gauthier Villars.
Bruno, I. J., Cole, J. C., Kessler, M., Luo, J., Motherwell, W. D. S., Purkis, L. H., Smith, B. R., Taylor, R., Cooper, R. I., Harris, S. E. & Orpen, A. G. (2004). *J. Chem. Inf. Comput. Sci.* **44**, 2133–2144.
Buist, A., Bonnaud, T., Edwards, R., Patterson, A. & Wright, M. (2021). United States Patent Application US 2021/0361626 A1.
Chen, M., Zhang, Y., Lu, F. & Zhang, X. (2016). International Patent Application WO 2016/131406 A1.
Dassault Systèmes. (2024). *BIOVIA Materials Studio 2025*. San Diego, CA. BIOVIA.
Donnay, J. D. H. & Harker, D. (1937). *Am. Mineral.* **22**, 446–467.
Dovesi, R., Erba, A., Orlando, R., Zicovich-Wilson, C. M., Civalleri, B., Maschio, L., Rérat, M., Casassa, S., Baima, J., Salustro, S. & Kirtman, B. (2018). *WIREs Comput. Mol. Sci.* **8**, e1360.
Erba, A., Desmarais, J. K., Casassa, S., Civalleri, B., Donà, L., Bush, I. J., Searle, B., Maschio, L., Edith-Daga, L., Cossard, A., Ribaldone, C., Ascrizzi, E., Marana, N. L., Flament, J.-P. & Kirtman, B. (2023). *J. Chem. Theory Comput.* **19**, 6891–6932.
Etter, M. C. (1990). *Acc. Chem. Res.* **23**, 120–126.
Favre-Nicolin, V. & Černý, R. (2002). *J. Appl. Cryst.* **35**, 734–743.
Friedel, G. (1907). *Bull. Soc. Française Minéral.* **30**, 326–455.
Gatti, C., Saunders, V. R. & Roetti, C. (1994). *J. Chem. Phys.* **101**, 10686–10696.
Gobechiya, E. R., Kabalov, Y. K., Orlova, A. I., Trubach, I. G., Bykov, D. M. & Kurazhkovskaya, V. S. (2004). *Crystallogr. Rep.* **49**, 390–395.
Groom, C. R., Bruno, I. J., Lightfoot, M. P. & Ward, S. C. (2016). *Acta Cryst.* B**72**, 171–179.
Hirshfeld, F. L. (1977). *Theor. Chim. Acta* **44**, 129–138.
Kabekkodu, S., Dosen, A. & Blanton, T. N. (2024). *Powder Diffr.* **39**, 47–59.
Kaduk, J. A., Crowder, C. E., Zhong, K., Fawcett, T. G. & Suchomel, M. R. (2014). *Powder Diffr.* **29**, 269–273.
Kim, S., Chen, J., Cheng, T., Gindulyte, A., He, J., He, S., Li, Q., Shoemaker, B. A., Thiessen, P. A., Yu, B., Zaslavsky, L., Zhang, J. & Bolton, E. E. (2023). *Nucleic Acids Res.* **51**, D1373–D1380.
Kresse, G. & Furthmüller, J. (1996). *Comput. Mater. Sci.* **6**, 15–50.
Leontowich, A. F. G., Gomez, A., Diaz Moreno, B., Muir, D., Spasyuk, D., King, G., Reid, J. W., Kim, C.-Y. & Kycia, S. (2021). *J. Synchrotron Rad.* **28**, 961–969.
Louër, D. & Boultif, A. (2014). *Powder Diffr.* **29**, S7–S12.
Macrae, C. F., Sovago, I., Cottrell, S. J., Galek, P. T. A., McCabe, P., Pidcock, E., Platings, M., Shields, G. P., Stevens, J. S., Towler, M. & Wood, P. A. (2020). *J. Appl. Cryst.* **53**, 226–235.
Materials Design. (2024). *MedeA 3.7.2*. Materials Design Inc., San Diego, USA.
MDI. (2025). *JADE Pro version 9.3*. Materials Data, Livermore, USA.
Motherwell, W. D. S., Shields, G. P. & Allen, F. H. (2000). *Acta Cryst.* B**56**, 857–871.
O'Boyle, N. M., Banck, M., James, C. A., Morley, C., Vandermeersch, T. & Hutchison, G. R. (2011). *J. Cheminf.* **3**, 33.
Palle, V. R. C., Bhat, R. P., Patel, P. K., Kumar, N. & Gregory, T. (2021). International Patent Application WO 2021/116901 A1.
Peintinger, M. F., Oliveira, D. V. & Bredow, T. (2013). *J. Comput. Chem.* **34**, 451–459.
Silk Scientific. (2013). *UN-SCAN-IT 7.0*. Silk Scientific Corporation, Orem, USA.
Spackman, P. R., Turner, M. J., McKinnon, J. J., Wolff, S. K., Grimwood, D. J., Jayatilaka, D. & Spackman, M. A. (2021). *J. Appl. Cryst.* **54**, 1006–1011.
Stephens, P. W. (1999). *J. Appl. Cryst.* **32**, 281–289.
Streek, J. van de & Neumann, M. A. (2014). *Acta Cryst.* B**70**, 1020–1032.
Sykes, R. A., McCabe, P., Allen, F. H., Battle, G. M., Bruno, I. J. & Wood, P. A. (2011). *J. Appl. Cryst.* **44**, 882–886.
Toby, B. H. & Von Dreele, R. B. (2013). *J. Appl. Cryst.* **46**, 544–549.
Tran, B. & Cohen, M. S. (2020). *Expert Opin. Drug. Discov.* **15**, 745–754.
Wavefunction, Inc. (2025). *Spartan '24. V. 1.3.1.* Wavefunction Inc., Irvine, USA.
Wheatley, A. M. & Kaduk, J. A. (2019). *Powder Diffr.* **34**, 35–43.

supporting information

Acta Cryst. (2026). E**82**, 639-644 [https://doi.org/10.1107/S2056989026004718]

Crystal structure of binimetinib (Form A), $C_{17}H_{15}BrF_2N_4O_3$, from synchrotron X-ray powder diffraction data and density functional theory

Jean guillaume Ducreux, James A. Kaduk, Anja Dosen and Thomas N. Blanton

Computing details

(binimetinib_3_phase_2)

Crystal data

$FeO_{22}P_3Zr_8$
M_r = 1230.51
Monoclinic, $P2_1/c$
a = 8.8395 Å
b = 8.9359 Å
c = 15.1869 Å
β = 125.16°
V = 980.73 Å^3
Z = 4
D_x = 8.334 Mg m^{-3}
T = 298 K

Refinement

Weighting scheme based on measured s.u.'s

Preferred orientation correction: March-Dollase correction coef. = 1.000 axis = [0, 0, 1]

Fractional atomic coordinates and isotropic or equivalent isotropic displacement parameters (Å^2)

	x	*y*	*z*	U_{iso}*/U_{eq}
Fe1	0.54200	0.20100	−0.17100	0.0139*
Zr2	0.13090	0.02910	−0.11940	0.0101*
Zr3	0.35780	0.03930	−0.39020	0.0127*
P4	−0.03800	0.25400	−0.50400	0.0127*
P5	0.24800	0.38200	−0.14700	0.0114*
P6	0.53100	0.39800	−0.35400	0.0127*
O7	−0.01200	0.32800	−0.58200	0.0165*
O8	−0.22200	0.17400	−0.57300	0.0165*
O9	−0.04000	0.35500	−0.42700	0.0139*
O10	0.12300	0.14400	−0.43200	0.0139*
O11	0.20400	0.22000	−0.17000	0.0215*
O12	0.30100	0.42400	−0.03500	0.0203*
O13	0.40100	0.40900	−0.16100	0.0177*
O14	0.08900	0.48300	−0.22700	0.0152*
O15	0.49900	0.24300	−0.32900	0.0165*
O16	0.69700	0.38900	−0.36000	0.0152*
O17	0.35600	0.45100	−0.46100	0.0152*
O18	0.56500	0.51900	−0.26800	0.0139*

(binimetinib_3_phase_1)

Crystal data

H_2KO_4P
M_r = 136.08
Orthorhombic, $P2_12_12_1$
a = 7.4487 (5) Å
b = 7.4626 (5) Å
c = 6.9755 (3) Å
V = 387.75 (4) Å^3
Z = 4
D_x = 2.331 Mg m^{-3}
T = 298 K

Refinement

Weighting scheme based on measured s.u.'s

Preferred orientation correction: March-Dollase correction coef. = 1.000 axis = [0, 0, 1]

Fractional atomic coordinates and isotropic or equivalent isotropic displacement parameters (Å^2)

	x	y	z	U_{iso}*/U_{eq}
P1	0.00000	0.25000	0.37500	0.0100*
K2	0.00000	0.25000	0.87500	0.0100*
O3	0.08970	0.40150	0.50060	0.0100*
O4	0.15570	1.16810	1.24930	0.0100*
O5	0.92620	1.10680	0.50530	0.0100*
O6	0.86180	0.33310	1.24490	0.0100*
H7	0.23200	0.39600	0.50300	0.0100*
H8	0.14600	1.02600	1.25700	0.0100*

6-(4-Bromo-2-fluoroanilino)-7-fluoro-*N*-(2-hydroxyethoxy)-3-methylbenzimidazole-5-carboxamide

(binimetinib_3_phase_0)

Crystal data

$C_{17}H_{15}BrF_2N_4O_3$
M_r = 441.23
Orthorhombic, $P2_12_12_1$
a = 23.1607 (11) Å
b = 16.0073 (11) Å
c = 4.86578 (17) Å
V = 1803.9 (2) Å^3
Z = 4
D_x = 1.625 Mg m^{-3}
Synchrotron radiation
T = 298 K
cylinder, 0.45 × 0.15 mm

Data collection

Wiggler Low Energy Beamline, Brockhouse X-ray Diffraction and Scattering Sector, Canadian Light Source diffractometer

Specimen mounting: Kapton capillary
Data collection mode: transmission
Scan method: step

Refinement

Weighting scheme based on measured s.u.'s

Preferred orientation correction: Simple spherical harmonic correction Order = 2 Coefficients: 0:0:C(2,0) = -0.416(16); 0:0:C(2,2) = -0.373(18)

Fractional atomic coordinates and isotropic or equivalent isotropic displacement parameters (Å^2)

	x	y	z	U_{iso}*/U_{eq}
Br1	0.2140 (2)	1.1878 (4)	0.6685 (13)	0.102 (4)*

F2	0.1638 (7)	0.7558 (12)	0.763 (4)	0.162 (7)*
F3	0.1628 (6)	0.8853 (7)	0.467 (3)	0.097 (8)*
O4	−0.1140 (6)	0.9111 (10)	0.360 (4)	0.271 (10)*
O5	−0.0394 (9)	0.8638 (15)	0.772 (3)	0.271 (10)*
O6	−0.2407 (14)	0.9150 (17)	0.579 (6)	0.271 (10)*
N7	0.0781 (5)	0.6083 (9)	0.073 (3)	0.162 (7)*
N8	0.0739 (7)	0.8714 (7)	0.828 (3)	0.097 (8)*
N9	0.1533 (6)	0.6159 (12)	0.362 (4)	0.162 (7)*
N10	−0.0612 (7)	0.8681 (15)	0.320 (3)	0.271 (10)*
C11	0.0672 (5)	0.6757 (12)	0.243 (4)	0.162 (7)*
C12	0.1152 (5)	0.6812 (9)	0.415 (3)	0.162 (7)*
C13	0.0721 (5)	0.8048 (8)	0.629 (4)	0.162 (7)*
C14	0.0224 (5)	0.7937 (9)	0.465 (4)	0.162 (7)*
C15	0.0191 (6)	0.7269 (11)	0.278 (5)	0.162 (7)*
C16	0.1161 (8)	0.7456 (16)	0.607 (6)	0.162 (7)*
C17	0.1321 (6)	0.5817 (14)	0.138 (5)	0.162 (7)*
C18	0.0347 (7)	0.5616 (15)	−0.082 (5)	0.162 (7)*
C19	−0.0326 (6)	0.8372 (8)	0.537 (3)	0.271 (10)*
C20	0.1037 (9)	0.9484 (8)	0.791 (5)	0.097 (8)*
C21	0.1489 (5)	0.9534 (6)	0.606 (3)	0.097 (8)*
C22	0.0928 (12)	1.0187 (11)	0.955 (7)	0.097 (8)*
C23	0.1845 (9)	1.0204 (8)	0.584 (6)	0.097 (8)*
C24	0.1232 (13)	1.0924 (10)	0.906 (7)	0.097 (8)*
C25	0.1697 (10)	1.0907 (8)	0.726 (6)	0.097 (8)*
C26	−0.1620 (8)	0.8543 (15)	0.313 (9)	0.271 (10)*
C27	−0.2166 (9)	0.9025 (19)	0.313 (5)	0.271 (10)*
H28	−0.02487	0.71766	0.16889	0.2456*
H29	0.05232	0.86998	1.03075	0.1171*
H30	0.15757	0.54516	−0.01714	0.2456*
H31	−0.01029	0.58209	−0.01501	0.2456*
H32	0.03773	0.49577	−0.02975	0.2456*
H33	0.03549	0.57555	−0.30781	0.2456*
H34	0.05590	1.02227	1.10109	0.1171*
H35	−0.04360	0.86005	0.10945	0.3252*
H36	0.22406	1.02131	0.43551	0.1171*
H37	0.11483	1.15369	1.03039	0.1171*
H38	−0.16330	0.80548	0.48347	0.3252*
H39	−0.15623	0.82195	0.10608	0.3252*
H40	−0.20864	0.96693	0.22067	0.3252*
H41	−0.24952	0.86822	0.18029	0.3252*
H42	0.22400	0.59610	0.45600	0.3252*

Geometric parameters (Å, º)

Br1—C25	1.883 (3)	C19—O5	1.231 (4)
F2—C16	1.347 (4)	C19—N10	1.343 (3)
F3—C21	1.322 (5)	C19—C14	1.492 (4)
O4—N10	1.417 (4)	C20—N8	1.422 (5)

O4—C26	1.454 (6)	C20—C21	1.386 (2)
O5—C19	1.231 (4)	C20—C22	1.403 (5)
O6—C27	1.421 (10)	C21—F3	1.322 (5)
O6—H42^{i}	0.85 (3)	C21—C20	1.386 (2)
N7—C11	1.380 (3)	C21—C23	1.357 (3)
N7—C17	1.359 (4)	C22—C20	1.403 (5)
N7—C18	1.462 (3)	C22—C24	1.394 (7)
N8—C13	1.439 (5)	C22—H34	1.113 (7)
N8—C20	1.422 (5)	C23—C21	1.357 (3)
N8—H29	1.107 (11)	C23—C25	1.366 (4)
N9—C12	1.392 (3)	C23—H36	1.167 (7)
N9—C17	1.317 (3)	C24—C22	1.394 (7)
N10—O4	1.417 (4)	C24—C25	1.385 (4)
N10—C19	1.343 (3)	C24—H37	1.170 (9)
N10—H35	1.110 (15)	C25—Br1	1.883 (3)
C11—N7	1.380 (3)	C25—C23	1.366 (4)
C11—C12	1.395 (3)	C25—C24	1.385 (4)
C11—C15	1.395 (4)	C26—O4	1.454 (6)
C12—N9	1.392 (3)	C26—C27	1.481 (9)
C12—C11	1.395 (3)	C26—H38	1.14 (4)
C12—C16	1.393 (2)	C26—H39	1.14 (3)
C13—N8	1.439 (5)	C27—O6	1.421 (10)
C13—C14	1.413 (3)	C27—C26	1.481 (9)
C13—C16	1.397 (3)	C27—H40	1.14 (3)
C14—C13	1.413 (3)	C27—H41	1.14 (3)
C14—C15	1.405 (3)	H28—C15	1.159 (10)
C14—C19	1.492 (4)	H29—N8	1.107 (11)
C15—C11	1.395 (4)	H30—C17	1.121 (13)
C15—C14	1.405 (3)	H31—C18	1.232 (16)
C15—H28	1.159 (10)	H32—C18	1.09 (3)
C16—F2	1.347 (4)	H33—C18	1.12 (3)
C16—C12	1.393 (2)	H34—C22	1.113 (7)
C16—C13	1.397 (3)	H35—N10	1.301 (15)
C17—N7	1.359 (4)	H36—C23	1.167 (7)
C17—N9	1.317 (3)	H37—C24	1.170 (9)
C17—H30	1.121 (13)	H38—C26	1.14 (4)
C18—N7	1.462 (3)	H39—C26	1.14 (3)
C18—H31	1.232 (16)	H40—C27	1.14 (3)
C18—H32	1.09 (3)	H41—C27	1.14 (3)
C18—H33	1.12 (3)	H42—O6^{ii}	0.85 (3)

N10—O4—C26	109.6 (3)	N7—C18—H33	113.1 (19)
C27—O6—H42^{i}	100 (3)	H31—C18—H33	104.3 (16)
C11—N7—C17	105.96 (9)	H32—C18—H33	114.8 (12)
C11—N7—C18	125.63 (16)	O5—C19—N10	122.8 (3)
C17—N7—C18	126.3 (3)	O5—C19—C14	119.2 (3)
C13—N8—C20	125.0 (4)	N10—C19—C14	114.1 (4)
C13—N8—H29	124.7 (9)	N8—C20—C21	119.9 (3)

C20—N8—H29	110.4 (9)	N8—C20—C22	122.5 (4)
C12—N9—C17	103.2 (2)	C21—C20—C22	117.4 (2)
O4—N10—C19	119.8 (3)	F3—C21—C20	118.0 (2)
O4—N10—H35	120.0 (10)	F3—C21—C23	117.6 (3)
C19—N10—H35	114.3 (9)	C20—C21—C23	123.8 (2)
N7—C11—C12	105.26 (15)	C20—C22—C24	119.3 (6)
N7—C11—C15	132.8 (2)	C20—C22—H34	122.8 (8)
C12—C11—C15	121.7 (3)	C24—C22—H34	117.1 (8)
N9—C12—C11	110.31 (13)	C21—C23—C25	117.3 (4)
N9—C12—C16	132.0 (3)	C21—C23—H36	122.4 (5)
C11—C12—C16	117.59 (18)	C25—C23—H36	120.1 (4)
N8—C13—C14	119.8 (3)	C22—C24—C25	119.0 (5)
N8—C13—C16	122.2 (3)	C22—C24—H37	122.4 (6)
C14—C13—C16	117.8 (2)	C25—C24—H37	118.1 (5)
C13—C14—C15	120.4 (3)	Br1—C25—C23	117.8 (2)
C13—C14—C19	120.22 (19)	Br1—C25—C24	120.1 (3)
C15—C14—C19	117.4 (5)	C23—C25—C24	122.07 (18)
C11—C15—C14	119.0 (3)	O4—C26—C27	109.1 (9)
C11—C15—H28	124.7 (7)	O4—C26—H38	110 (3)
C14—C15—H28	116.2 (7)	C27—C26—H38	110 (2)
F2—C16—C12	118.6 (2)	O4—C26—H39	109 (3)
F2—C16—C13	118.3 (4)	C27—C26—H39	110 (3)
C12—C16—C13	122.8 (2)	H38—C26—H39	109.5 (17)
N7—C17—N9	113.8 (2)	O6—C27—C26	114.1 (11)
N7—C17—H30	119.5 (10)	O6—C27—H40	107 (3)
N9—C17—H30	125.4 (9)	C26—C27—H40	109.4 (19)
N7—C18—H31	107.9 (7)	O6—C27—H41	109 (2)
N7—C18—H32	109.4 (14)	C26—C27—H41	109 (2)
H31—C18—H32	107 (2)	H40—C27—H41	108.6 (15)

Symmetry codes: (i) $x-1/2, -y+3/2, -z+1$; (ii) $x+1/2, -y+3/2, -z+1$.

(binimetinib_VASP)

Crystal data

$C_{17}H_{15}BrF_2N_4O_3$
$M_r = 441.23$
Orthorhombic, $P2_12_12_1$
$a = 23.16240$ Å
$b = 16.01200$ Å
$c = 4.86608$ Å
$V = 1804.71$ Å^3
$Z = 4$

Data collection

$h = \rightarrow$
$k = \rightarrow$
$l = \rightarrow$

Fractional atomic coordinates and isotropic or equivalent isotropic displacement parameters (Å^2)

	x	y	z	B_{iso}*/B_{eq}
Br1	0.21583	1.19671	0.75423	
F2	0.17429	0.77297	0.66775	
F3	0.16697	0.90877	0.32040	

O4	−0.10831	0.89653	0.26129
O5	−0.04005	0.85262	0.68214
O6	−0.21696	0.91024	0.54783
N7	0.09310	0.60081	0.01736
N8	0.07664	0.87294	0.71560
N9	0.17259	0.63256	0.26145
N10	−0.05892	0.84888	0.22432
C11	0.07868	0.67001	0.17370
C12	0.12943	0.68901	0.32456
C13	0.07819	0.80469	0.53543
C14	0.02728	0.78152	0.38710
C15	0.02719	0.71394	0.20461
C16	0.12781	0.75578	0.50880
C17	0.14903	0.58161	0.07714
C18	0.05533	0.55671	−0.17077
C19	−0.02660	0.82946	0.44334
C20	0.10956	0.94556	0.71049
C21	0.15473	0.96344	0.52698
C22	0.09601	1.00905	0.90051
C23	0.18688	1.03650	0.53834
C24	0.12630	1.08382	0.91226
C25	0.17252	1.09668	0.73321
C26	−0.15852	0.84578	0.19082
C27	−0.21257	0.89367	0.26039
H28	−0.01202	0.69634	0.09477
H29	0.03603	0.88130	0.79338
H30	0.17098	0.52878	−0.01938
H31	0.01541	0.53825	−0.06465
H32	0.07718	0.50010	−0.24257
H33	0.04410	0.59684	−0.34606
H34	0.06091	0.99782	1.04600
H35	−0.04755	0.83869	0.02052
H36	0.22171	1.04588	0.39098
H37	0.11482	1.13114	1.06363
H38	−0.15639	0.78740	0.30960
H39	−0.15748	0.83253	−0.03098
H40	−0.21384	0.95254	0.14206
H41	−0.24900	0.85504	0.18852
H42	−0.25621	0.89297	0.61096

Hydrogen-bond geometry (Å, º)

D—H···*A*	*D*—H	H···*A*	*D*···*A*	*D*—H···*A*
N8—H29···O5	1.02	1.90	2.727	136
N10—H35···O5^{i}	1.04	1.67	2.675	161
O6—H42···N9^{ii}	1.00	1.81	2.806	176
C17—H30···O6^{iii}	1.09	2.18	3.221	158
C18—H32···O5^{iii}	1.10	2.53	3.288	125

C26—H38···Br1^{iv}	1.10	2.92	3.841	142
C26—H39···Br1^{iii}	1.10	2.78	3.486	122

Symmetry codes: (i) x, y, $z-1$; (ii) $x-1/2$, $-y+3/2$, $-z+1$; (iii) $-x$, $y-1/2$, $-z+1/2$; (iv) $-x$, $y-1/2$, $-z+3/2$.